

FACTOR OF SAFETY BY THE STRENGTH-REDUCTION TECHNIQUE APPLIED TO THE HOEK–BROWN MODEL

O. Ledesma^{a,b}, I. García Mendive^b and A. Sfriso^{a,b}

^aUniversity of Buenos Aires, onledesma@fi.uba.ar, materias.fi.uba.ar/6408

^aSRK Consulting (Argentina), Chile 300, CABA, latam.srk.com

Keywords: Hoek–Brown, Finite Element, Strength-Reduction Technique, Non-Associativity, Dilatancy.

Abstract. This paper describes the implementation of the Hoek–Brown model as a perfect elastoplasticity model in a finite element code. The yield function is a standard Mohr–Coulomb surface incorporating a stress-dependent friction angle which accomplishes an exact reproduction of the Hoek–Brown strength envelope for all stress states. The formulation of the model is performed in such a way as to allow for a direct implementation of the shear strength-reduction technique in order to calculate the factor of safety of boundary-value problems. The efficiency of the numerical algorithm is discussed, with emphasis in the effect of the numerical implementation of three dilatancy models: deviatoric associativity, full non-associativity employing a Mohr–Coulomb shaped plastic potential and radial return. A comparison is presented between the results obtained for slope stability analyses using limit equilibrium methods and the built-in Hoek–Brown model available in Plaxis. Finally, the application of the model to an excavation for an underground mine in Uruguay is presented and discussed.

1 INTRODUCTION

The Hoek–Brown failure criterion was introduced in 1980 as an empirical estimate of the strength of rock masses which takes into account the properties of the intact rock and those of the discontinuities (Hoek & Brown, 1980a) (Hoek & Brown, 1980b). Filling a gap that existed at that time, the Hoek–Brown criterion was almost universally adopted as a full yield criterion for a number of conventional elastoplasticity models in rock engineering, extending its use far beyond its initial scope. Best-fit conversion equations between the Hoek–Brown criterion and the Mohr–Coulomb criterion were proposed, based on different assumptions and aiming at different objectives, e.g. (Hammah, Yacoub, Corkum, & Curran, 2005). All these formulas are found ubiquitously in engineering reports and employed for the computation of factors of safety of a number of rock engineering designs.

In computational geomechanics, factors of safety are generally computed by the strength-reduction technique, where shear strength parameters are reduced monotonically until convergence of the boundary-value problem is no longer achieved. The lowest reduction factor producing non-convergence is reported as the “factor of safety” of the boundary-value problem. The implementation of this strength-reduction technique is straightforward for the conventional Mohr–Coulomb criterion but is more obscure for other strength criteria having a curved failure envelope in stress-space. Hoek–Brown criterion is one of such criteria, explaining why different implementations of the Hoek–Brown model yield different factors of safety for a given boundary-value problem, and why it is difficult to make any of those models match the result obtained by the Mohr–Coulomb criterion even if a considerable calibration effort is made, e.g. (Benz, Schwab, Kautner, & Vermeer, 2008). The re-formulation of the Hoek–Brown criterion as a nonlinear Mohr–Coulomb criterion allows for establishing of a consistent procedure for computing factors of safety in computational rock engineering.

Another issue affecting the reliability and reproducibility of calculations is the choice and numerical implementation of dilatancy models. Non-associativity of geomaterials is experimentally supported by the fact that, after large-enough deformation, shear continues at constant volume for a material that has a cone-shaped yield function. This elementary fact does not necessarily imply that non-associativity should be extended to deviatoric plastic strain, a feature often observed in commercial codes which either employ the Mohr–Coulomb function as a plastic potential, e.g. Plaxis, using (de Borst, 1987) or use other ad-hoc non-associativity expressions aimed at simplifying time-integration, e.g. FLAC (Itasca Consulting Group, 1998).

This paper revisits the Hoek–Brown criterion, introduces its re-formulation as a Mohr–Coulomb criterion with a stress-dependent friction angle yielding a curved cone and presents its numerical implementation in the finite-element code Plaxis. Three different non-associativity formulations are discussed and compared: deviatoric associativity & volumetric non-associativity, full non-associativity (de Borst, 1987) and full non-associativity with a radial return scheme.

The model is compared with the standard Hoek–Brown model available in Plaxis (Brinkgreve, Kumarswamy, & Swolfs, 2016) and plane-strain compression, showing the impact of the dilatancy formulation on the outcome of the model. Then, the exercise of computing the factor of safety of a rock slope is performed five times, namely by employing the analytic method of slices, the Plaxis built-in Hoek–Brown model and the three variants of the Hoek–Brown model introduced in this paper. The practical implications of the results obtained are discussed shortly. Finally, an example is given of the application of the Hoek–Brown implementation proposed in this paper to the case history problem of an underground excavation for a gold mine in Uruguay (García Mendive, Sterin, & Rellan, 2016).

2 HOEK–BROWN CONSTITUTIVE MODEL

2.1 The Hoek–Brown failure criterion (2002 version)

The Hoek–Brown failure criterion was introduced in 1980 (Hoek & Brown, 1980a) (Hoek & Brown, 1980b) and was extended in 2002 to its current form (Hoek, Carranza, & Corkum, 2002). In principal stresses $\{\sigma_1, \sigma_2, \sigma_3\}$ (compression negative but $\sigma_1 \leq \sigma_2 \leq \sigma_3$) it reads

$$f_{HB} = \sigma_3 - \sigma_1 - \sigma_c \left(s - m \frac{\sigma_3}{\sigma_c} \right)^a = 0 \quad (1)$$

where m , s , a are material parameters and σ_c is the unconfined compression strength of the intact rock. The rationale behind the practical use of this criterion for intact rock-cores with no discontinuities is: i) the unconfined compression strength σ_c and the uniaxial tensile strength σ_t are measured; ii) parameter m is defined as $m = \sigma_c/\sigma_t$; iii) parameter s is set to $s = 1$; and iv) parameter a is computed as best-fit of experimental data, but $a = 0.50$ for all practical purposes. For rock-masses exhibiting several sets of discontinuities, only σ_c can be actually measured. The rest of the material parameters must be adopted based on charts, experimental fits or back-analysis of rock-mass behavior. For a complete discussion on the Hoek–Brown criterion, see (Hoek, Carranza, & Corkum, 2002) (Eberhardt, 2012).

Figure 1 shows different views of the yield criterion given by eqn. (1), showing that it is aimed to predict failure in shear at high mean stress, combined tensile-shear failure and pure tension. In Figure 1, $p = -(\sigma_1 + \sigma_2 + \sigma_3)/3$ is mean pressure, τ is the shear stress acting on a given plane and σ_n is the normal stress acting on the same plane – the standard Mohr plot.

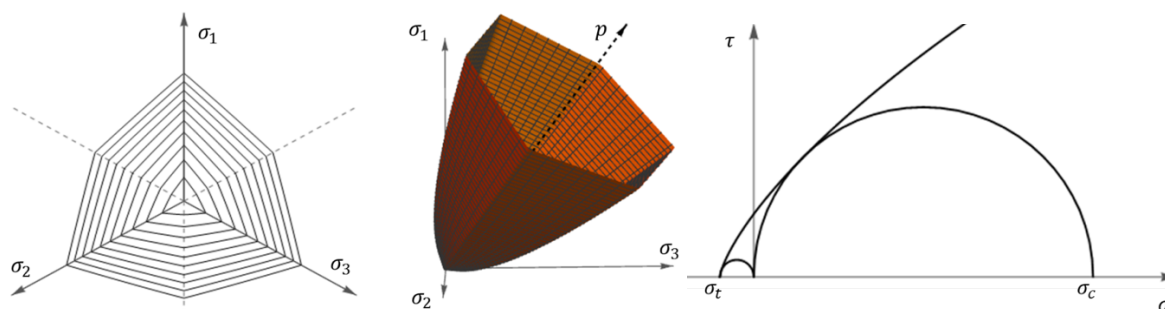


Figure 1: Hoek-Brown yield criterion. a) deviatoric plot. b) 3D plot. c) Mohr plot.

2.2 The Hoek-Brown perfect plasticity model

The Hoek-Brown failure criterion is the yield surface of a full perfect-plasticity constitutive model which is implemented in most numerical codes for computational geomechanics, like Plaxis, RS² (before, Phase²), FLAC, etcetera. The outline of the model, as reported in software manuals, is listed below.

One state variable, the effective stress σ , is employed. Standard additive decomposition of the infinitesimal strain ϵ into elastic strain ϵ^e and plastic strain ϵ^p is adopted

$$\epsilon = \epsilon^e + \epsilon^p \quad (2)$$

The stress-strain equation is that of isotropic linear elasticity

$$\dot{\sigma} = \mathbf{D} : \dot{\epsilon}^e \quad (3)$$

where σ is the effective stress tensor and \mathbf{D} is the fourth order isotropic elasticity tensor, a function of the material parameters E , the Young's modulus, and ν , the Poisson's ratio. The yield function is given by eqn (1). The plastic strain-rate tensor is

$$\dot{\epsilon}^p = \dot{\lambda} \mathbf{m} \quad (4)$$

where $\dot{\lambda}$ is a plastic multiplier and \mathbf{m} is the direction of plastic strain-rate computed in different ways by different codes as will be discussed below. The standard switching condition is employed

$$\dot{\lambda} = \begin{cases} \dot{\lambda} & \text{if } f_{HB} = 0 \wedge \dot{f}_{hb} > 0 \\ 0 & \text{otherwise} \end{cases} \quad (5)$$

Being a perfect plasticity model, no internal variables or evolution equations are defined.

2.3 Hoek-Brown surface is not a curved Mohr-Coulomb surface

The Hoek-Brown yield surface is not a Mohr-Coulomb cone that curves as a function of mean stress, the deviatoric plot shown in Figure 1a is misleading. As the curvature shown in Figure 1b and Figure 1c is a function of σ_3 and σ_3 is not the same for the extension and compression corners of a given deviatoric plane, the aspect ratio of the Hoek-Brown criterion cannot be reproduced by the Mohr-Coulomb criterion. Moreover, the lines connecting corners in Figure 1a are not straight but slightly convex (convexity accomplished by chance). Both issues are schematically shown in Figure 2.

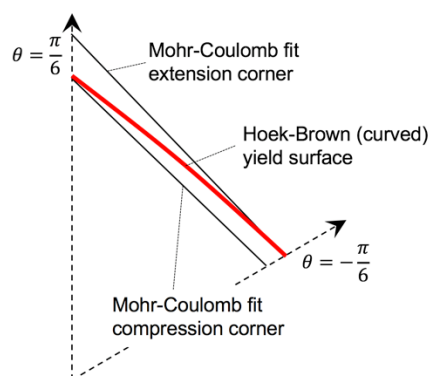


Figure 2: Deviatoric plot of Hoek-Brown yield surface and Mohr-Coulomb matches for both corners.

3 FACTOR OF SAFETY

3.1 Definitions

In classical soil mechanics, the factor of safety is the ratio of the shear strength at the plane of potential failure τ_f and the shear stress acting in the same plane τ , namely

$$F_a = \frac{\tau_f}{\tau} \quad (6)$$

For the Mohr–Coulomb criterion, eqn. (6) reads

$$F_a = \frac{c + \sigma_n \tan(\phi)}{\tau} \quad (7)$$

where c is the cohesion and ϕ is the friction angle, material parameters of the Mohr–Coulomb criterion. In the framework of computational geomechanics, application of eqn. (7) is not practical, as the concept of “failure plane” is lost in favor of a full continuum mechanics approach. The strength-reduction technique is employed instead.

For the Mohr–Coulomb model, a “reduced” set of material parameters c^* and ϕ^* is computed

$$\begin{aligned} c^* &= c/F_n \\ \tan(\phi^*) &= \tan(\phi)/F_n \end{aligned} \tag{8}$$

The boundary-value problem is then solved using this set of reduced material parameters while keeping all other parameters unchanged. If convergence is obtained, the F_n value is increased and the problem is solved again. The lowest F_n producing non-convergence is reported as the “factor of safety” of the problem.

Eqns. (7) and (8) yield widely different values for most problems in routine geomechanics (Sfriso A. O., 2008). For instance, Figure 3 shows that for a triaxial compression test of a sand having $\phi = 30^\circ$, a sample that would yield $F_a = 2.00$ using eqn. (7) yields $F_n = 1.63$ if eqn. (8) is employed.

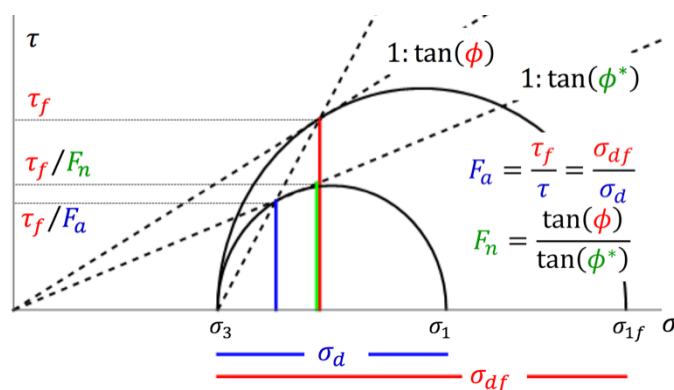


Figure 3: Factors of safety after eqn. (7) and (8).

3.2 Shear strength-reduction technique applied to the Mohr–Coulomb model

In principal stresses, the Mohr–Coulomb criterion reads

$$f_{MC} = \sigma_3 - \sigma_1 + (\sigma_1 + \sigma_3) \sin(\phi) - 2c \cos(\phi) = 0 \tag{9}$$

The apex of the Mohr–Coulomb cone defined by eqn. (9) is obtained by imposing $\sigma_1 = \sigma_3$. It yields

$$\sigma_3^{apex} = c_p = \frac{c}{\tan(\phi)} \tag{10}$$

where the derived parameter c_p is introduced. A quick inspection of eqn. (10) bearing in mind eqn. (8) shows that c_p remains unchanged during the strength-reduction process because both the numerator and denominator of the right-hand ratio are reduced by the same F_n . This means that the Mohr–Coulomb cone shrinks in stress-space keeping the position of its apex unchanged. Eqn. (9) can be thus conveniently re-written in the form

$$f_{MC} = \sigma_3 - \sigma_1 + (\sigma_1 + \sigma_3 - 2c_p) \sin(\phi) = 0 \tag{11}$$

For computing F_n , $\sin(\phi)$ is replaced by $\sin(\phi^*)$ which can be derived from eqn. (8b)

$$\sin(\phi^*) = \frac{\tan(\phi)}{\sqrt{F_n^2 + \tan^2(\phi)}} \tag{12}$$

The boundary-value problem is now solved using ϕ^* as a material parameter instead of ϕ , and increasing F_n until convergence is no longer achieved.

3.3 Shear strength-reduction technique for the Hoek–Brown model in Plaxis

The ease of implementing the strength-reduction technique in eqn. (9) and the difficulties associated to doing it in eqn. (1) is apparent. The problem of determining which parameters to reduce in the latter and how to do it has several solutions yielding different factors of safety for the same boundary-value problem.

In Plaxis (Benz, Schwab, Kauther, & Vermeer, 2008), the Hoek Brown yield function is reformulated by including a material strength reduction factor η

$$\begin{aligned} f_{HB} &= \sigma_3 - \sigma_1 - \tilde{f}_d(\sigma_3) \\ \tilde{f}_d &= \frac{\sigma_c}{\eta} \left(-m \frac{\sigma_3}{\sigma_c} + s \right)^a \end{aligned} \quad (13)$$

In order to derive an expression for η , a tangentially fitted Mohr-Coulomb criterion in $q - p$ space and triaxial loading is considered. In such conditions

$$\begin{aligned} p &= -\frac{\sigma_1 + 2\sigma_3}{3} \\ q &= \sigma_3 - \sigma_1 \end{aligned} \quad (14)$$

which can be substituted in eqn. (13) and used to compute the slope $\partial q / \partial p$ which is equated to that of the Mohr-Coulomb criterion

$$\frac{\partial q}{\partial p} = \frac{3\tilde{f}'_d}{3 + \tilde{f}'_d} = \frac{6 \sin(\phi_t)}{3 - \sin(\phi_t)} \quad (15)$$

which yields the expression for the tangential-fit friction angle ϕ_t

$$\sin(\phi_t) = \frac{\tilde{f}'_d}{2 + \tilde{f}'_d} \quad (16)$$

In eqn. (16), \tilde{f}'_d is a function of η while ϕ_t is a function of F_n , and therefore a closed-form expression for η as a function of F_n can be obtained (Benz, Schwab, Kauther, & Vermeer, 2008)

$$\eta = \sqrt{F_n^2 (1 + \tilde{f}'_d) + \tilde{f}'_d{}^2} - \frac{\tilde{f}'_d}{2} \quad (17)$$

It is worth noting (Benz, Schwab, Kauther, & Vermeer, 2008) that considering triaxial extension yields the same result.

3.4 Shear strength-reduction technique for the Hoek–Brown model in RS²

In RS² (Hammah, Yacoub, Corkum, & Curran, 2005), the strength reduction scheme is established in terms of the shear strength at the plane of potential failure

$$\tau_f^* = \frac{\tau_f}{F_n} \quad (18)$$

where

$$\tau_f = (\sigma_3 - \sigma_1) \frac{\sqrt{1 + a m \left(-m \frac{\sigma_3}{\sigma_c} + s \right)^{a-1}}}{2 + a m \left(-m \frac{\sigma_3}{\sigma_c} + s \right)^{a-1}} \quad (19)$$

In order to determine the reduced parameters that correspond to τ_f^* it is assumed that

$$\sigma_c^* = \frac{\sigma_c}{F_n} \quad (20)$$

The remaining parameters are estimated by minimizing the error between τ_f^* and τ_f/F_n

$$\min \left(\int_{\sigma_t}^{\sigma_{n,max}} \left(\tau_f^* - \frac{\tau_f}{F_n} \right) d\sigma_n \right) \quad (21)$$

where $\sigma_{n,max}$ is the normal stress at the failure plane calculated for the maximum σ_3 found in the boundary-value problem

$$\sigma_{n,max} = -\frac{1}{2}(\sigma_1 + \sigma_3) - \frac{1}{2}(\sigma_3 - \sigma_1) \frac{am \left(-m \frac{\sigma_3}{\sigma_c} + s \right)^{a-1}}{2 + am \left(-m \frac{\sigma_3}{\sigma_c} + s \right)^{a-1}} \Bigg|_{\sigma_3=\sigma_{3,max}} \quad (22)$$

and σ_1 is to be expressed in terms of σ_3 by means of eqn. (1). Note that this implementation yields a conversion technique that depends on the size of the mesh, as a higher mesh would have a higher $\sigma_{n,max}$ thus changing the result of the minimization of eqn. (21).

It is not surprising that the procedures described in sections 3.3 and 3.4 yield different results which cannot be compared or converted one into another. This is a major issue which is affecting the understanding of the results of numerical models by practitioners.

4 THE HOEK–BROWN MODEL AS A MOHR–COULOMB MODEL WITH $\phi(\sigma_3)$

4.1 Derivation

The objective is to rewrite eqn. (1) as eqn. (11) with a stress-dependent friction angle $\phi(\sigma_3)$, by obtaining suitable relationships between c_p , $\sin(\phi(\sigma_3))$ and the Hoek–Brown parameters. To solve for c_p , the apex of both criteria, eqn. (1) and eqn. (11), are forced to match. For the Hoek–Brown criterion, eqn. (1), σ_3 at the apex is

$$\sigma_3^{apex} = \sigma_c \frac{s}{m} \quad (23)$$

while for the Mohr–Coulomb criterion eqn. (10) holds. Mohr–Coulomb parameter c_p is obtained by equating both expressions

$$c_p = \sigma_c \frac{s}{m} \quad (24)$$

To derive a function $\sin(\phi(\sigma_3))$ enforcing $f_{HB} \equiv f_{MC}$ in the whole stress-space, the auxiliary variable $\sigma_d = \sigma_3 - \sigma_1$ is defined and solved for in both eqn. (1)

$$\sigma_d = \sigma_c \left(s - m \frac{\sigma_3}{\sigma_c} \right)^a \quad (25)$$

and eqn. (11)

$$\sigma_d = \frac{2(c_p - \sigma_3) \sin(\phi)}{1 - \sin(\phi)} \quad (26)$$

Inserting eqn. (24) in eqn. (26), equating the result with eqn. (25) and solving for $\sin(\phi)$ yields

$$\sin(\phi(\sigma_3)) = \frac{1}{1 + \omega} \quad (27)$$

where the auxiliary function

$$\omega(\sigma_3) = \frac{2}{m} \left(s - \frac{m \sigma_3}{\sigma_c} \right)^{1-a} \quad (28)$$

is introduced for ease of reading. The Hoek–Brown yield function is finally rewritten in the form

$$f_{HB} = \sigma_3 - \sigma_1 + \left(\sigma_1 + \sigma_3 - 2\sigma_c \frac{s}{m} \right) \frac{1}{1 + \omega} = 0 \quad (29)$$

It must be noted that eqn. (29) yields $\phi = 90^\circ$ at σ_3^{apex} , effectively reproducing the smooth cap closure of the Hoek–Brown criterion in pure tension.

4.2 Shear strength-reduction technique

The application of the strength-reduction technique to eqn.(29) is straight-forward. After eqn. (27) and some algebra, $\tan(\phi(\sigma_3))$ is computed to be

$$\tan(\phi(\sigma_3)) = \frac{1}{\sqrt{\omega(2 + \omega)}} \quad (30)$$

Eqn. (30) is replaced in eqn. (12) to yield

$$\sin(\phi^*(\sigma_3)) = \frac{1}{\sqrt{1 + \omega(2 + \omega)F_n^2}} \quad (31)$$

The advantage of this formulation is that eqn. (31) exactly reproduces the rationale behind the strength-reduction approach for the Hoek–Brown criterion and therefore produces factors of safety that are entirely comparable to those obtained by analytical methods or numerical methods employing the Mohr–Coulomb model.

Figure 4 shows the Hoek-Brown criterion in the normalized $\tau/\sigma_c - \sigma/\sigma_c$ Mohr plot for $m = 20$, $s = 0.2$, $a = 0.5$, $\sigma_c = 50MPa$, the corresponding Mohr's circle for the unconfined compression test, and the result of eqns. (29) and (30) for $F_n = 1.5$ and $F_n = 2.0$.

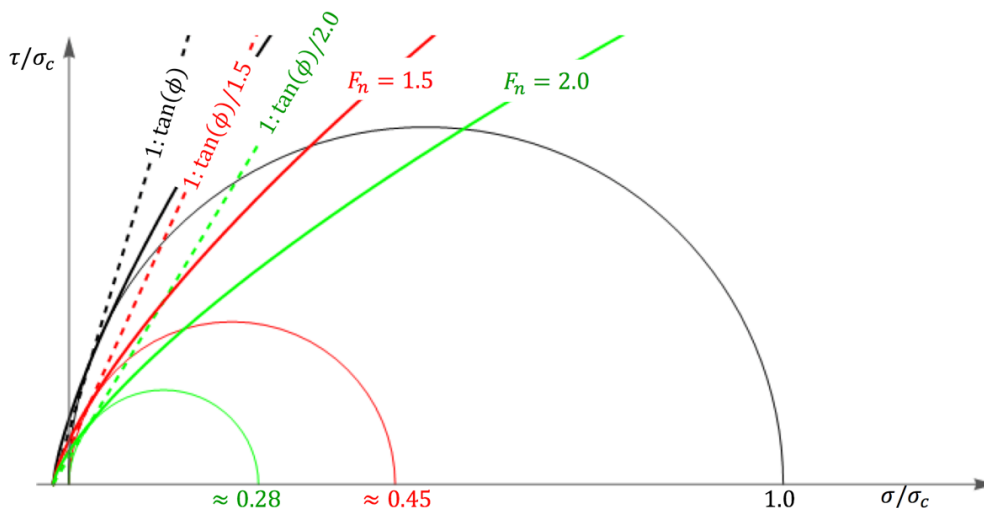


Figure 4: Hoek-Brown criterion in normalized $\tau/\sigma_c - \sigma/\sigma_c$ plot.

5 DILATANCY AND NON-ASSOCIATIVITY

5.1 Full non-associativity

The definition of the plastic strain rate unit tensor \mathbf{m} is commonly based on a scalar function of stress $g(\boldsymbol{\sigma})$ so called plastic potential

$$\mathbf{m} = \partial g / \partial \boldsymbol{\sigma} \quad (32)$$

Full associativity is obtained when the plastic potential $g(\boldsymbol{\sigma})$ matches the yield function $f(\boldsymbol{\sigma})$, namely

$$\mathbf{m} = \mathbf{n} = \partial f / \partial \boldsymbol{\sigma} \quad (33)$$

where \mathbf{n} is the normal to $f(\boldsymbol{\sigma})$ in stress-space. Despite a number of arguments supporting the theoretical soundness of associative plasticity, it has long been abandoned in computational geomechanics as it yields non-physical results – way-off too much dilatancy.

Non-associativity is obtained when $g \neq f$. For instance, the Vermeer-DeBorst (de Borst, 1987) non-associative formulation is often employed in the Mohr-Coulomb model by adopting

$$g = \sigma_3 - \sigma_1 + (\sigma_1 + \sigma_3) \sin(\psi) \quad (34)$$

where the dilatancy angle ψ replaces the friction angle ϕ in eqn. (11).

5.2 Deviatoric associativity

A special subset of non-associativity is volumetric-only non-associativity, preserving associativity in deviatoric stress-space. In formulas

$$\mathbf{n}_d = \mathbf{I}^d : \frac{\partial f}{\partial \boldsymbol{\sigma}} \quad (35)$$

$$\mathbf{m}_d = \frac{\mathbf{n}_d}{\|\mathbf{n}_d\|} \quad (36)$$

$$\mathbf{m} = \mathbf{m}_d + \beta \mathbf{1} \quad (37)$$

where \mathbf{I}^d is the fourth-order deviatoric projector, \mathbf{m}_d and \mathbf{n}_d are the deviatoric parts of \mathbf{m} and \mathbf{n} , and β is a dilatancy term. This particular form of non-associativity has been employed in a number of constitutive models for geomaterials that employ smooth J_3 yield functions for soils (e.g. (Sfriso, Weber, & Nuñez, 2011) (Macari, Weihe, & Arduino, 1997) (Collins, 2005) (Kim & Lade, 1988), and for concrete (e.g., (Etse & Willam, 1996)).

Deviatoric associativity is appealing: eigenvectors of \mathbf{m} match those of the deviatoric stress \mathbf{s} , as in associative models; most of the theoretical arguments supporting associativity still prevail for deviatoric-associative models; and it allows for a straight-forward implementation of generalized stress-dilatancy equations in principal stress-space (Sfriso, Weber, & Nuñez, 2011) (Pivonka & Willam, 2003). (Sfriso & Weber, 2010).

The final word on the choice of a flow rule should be given by experimental results. Unfortunately, true triaxial testing of geomaterials in the failure region has proven to be extremely challenging. Discrete element simulations (DEM) of 3D tests of bonded geomaterials support the deviatoric associativity concept, at least for monotonic loading. Figure 5 [modified from (Phusing, Suzuk, & Zaman, 2016)] shows one example of such DEM simulation, showing that strain increments are effectively close to normal to the (curved) yield surface. However, deviatoric associativity applied to yield surfaces having edges poses challenges, as shall be shown below.

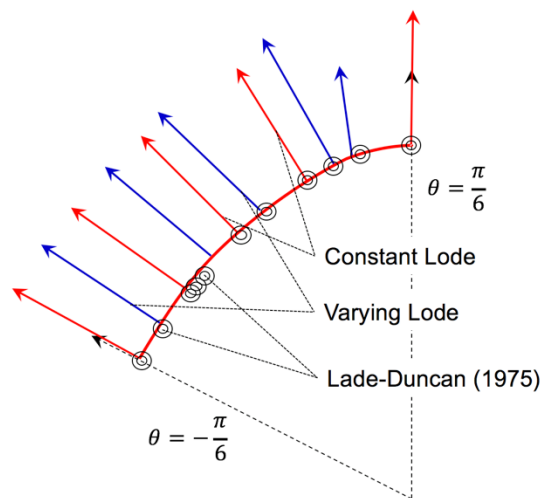


Figure 5: DEM simulation of plastic strain direction at failure, modified from (Phusing, Suzuk, & Zaman, 2016).

5.3 Stress-dependent dilatancy

Dilatancy is pressure-dependent for all granular geomaterials due to contact crushing. Cemented geomaterials like intact rocks also show pressure-dependent dilatancy, as they exhibit high dilation at low pressure – mainly as a result of micro-defect induced cracking – and a ductile behavior at high pressure. Rock masses, having pre-existing joints and macro-defects, show as similar pattern, albeit the rate of dilation is smaller than those of intact rocks at low pressure.

Dilatancy is, in fact, full stress-dependent, in the sense that dilation rate depends also on the Lode's angle. For unbonded geomaterials, the subject was originally raised by Rowe (Rowe P. , 1962) (Rowe P. , 1971) and subsequently studied by other researchers. Few dilatancy models fully address real 3D stress-paths. Guo and Stolle (Guo & Stolle, 2004), Guo and Wan (Guo & Wan, 2007) and Sfriso and Weber (Sfriso & Weber, 2010) introduced numerical implementations of Rowe's equation for sands. Tsegaye and Benz (Tsegaye & Benz, 2014) also introduced a general stress-dilatancy formulation and applied it to the Hoek–Brown criterion. Sfriso et al (Sfriso, Weber, & Nuñez, 2011) further discussed the numerical implications of the use of a 3D dilatancy formulation. Figure 6 shows the dependence of β on Lode's angle resulting from Rowe's formulation (Sfriso & Weber, 2010).

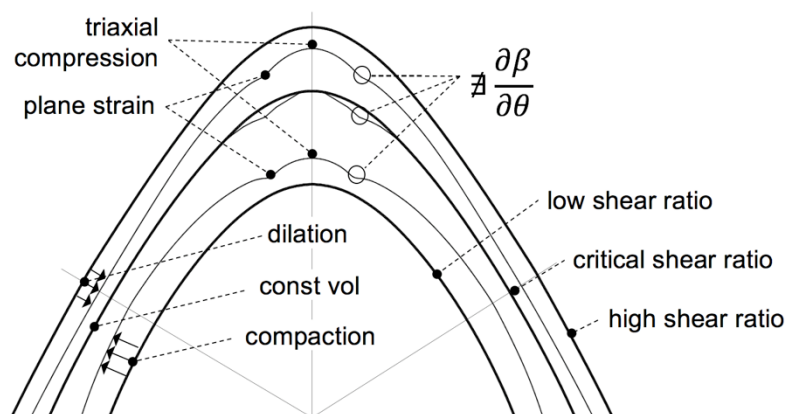


Figure 6: Implementation of Rowe's full stress-dependent dilatancy model, modified from (Sfriso, Weber, & Nuñez, 2011).

5.4 Flow rules for the Hoek-Brown criterion available in commercial software

As eqn (1) was introduced just as an empirical failure criterion for analytical purposes, no “original” plastic potential was defined, allowing each software developer to employ its own set of flow rules. For the Hoek-Brown criterion, numerical implementations available in commercial software employ full-associativity. Examples are given below for two popular software products in computational geomechanics.

In FLAC (Itasca Consulting Group, 1998), a stress-dependent scalar γ relates the increment of principal plastic strain components and therefore defines the direction of plastic strain

$$\dot{\epsilon}_1^p = \gamma \dot{\epsilon}_3^p \quad (38)$$

For uniaxial stress ($\sigma_3 \approx 0$), an associated flow rule is adopted, aiming at reproducing the high dilation produced by cracking and wedging of rock blocks during sample failure. In principal stresses

$$\dot{\epsilon}_i^p = \lambda \frac{\partial F}{\partial \sigma_i} \quad (39)$$

and γ is computed to be

$$\gamma_{af} = \frac{1}{1 + am(s - m \sigma_3/\sigma_c)^{a-1}} \quad (40)$$

In uniaxial tension, a radial flow rule is adopted, yielding

$$\gamma_{rf} = \frac{\sigma_1}{\sigma_3} \quad (41)$$

At a confining pressure σ_3^{cv} – a new material parameter of the model – constant volume plastic shearing is assumed, and therefore

$$\gamma_{cv} = -1 \quad (42)$$

Finally, the general flow rule is the combination of eqn. (38) and the linear interpolation of the above-mentioned eqns. (40), (41) and (42)

$$\gamma = \frac{1}{\frac{1}{\gamma_{af}} + \left(\frac{1}{\gamma_{cv}} - \frac{1}{\gamma_{af}}\right) \frac{\sigma_3}{\sigma_3^{cv}}} \quad \text{if } \sigma_3 > \sigma_3^{cv} \quad (43)$$

$$\gamma = -1 \quad \text{otherwise}$$

In Plaxis, a different approach is proposed (Brinkgreve, Kumarswamy, & Swolfs, 2016). A “transformed stress”

$$S_i = \frac{-\sigma_i}{m \sigma_c} + \frac{s}{m^2} \quad (44)$$

is defined for each principal stress σ_i . The flow rule is then defined as

$$g_{13} = S_1 - \frac{1 + \sin(\psi_{mob})}{1 - \sin(\psi_{mob})} S_3$$

$$g_{12} = S_1 - \frac{1 + \sin(\psi_{mob})}{1 - \sin(\psi_{mob})} S_2 \quad (45)$$

where

$$\psi_{mob} = \frac{\sigma_3^{cv} + \sigma_3}{\sigma_3^{cv}} \psi \geq 0 \quad (46)$$

is the mobilized dilatancy angle computed after the material parameters ψ (measured in an unconfined compression test) and σ_3^{cv} . In the tensile zone, Plaxis implementation of the Hoek–Brown model uses the expression

$$\psi_{mob} = \psi + \frac{\sigma_3}{\sigma_t} (90^\circ - \psi) \quad (47)$$

yielding a dilatancy angle of 90° in isotropic tension. It must be noted that full non-associativity is employed, bearing in mind ease of implementation rather than physics, and that the concept of dilatancy as the volume change induced by plastic shearing has been extended to uniaxial tension plasticity in the two models described.

6 NUMERICAL IMPLEMENTATION

6.1 Algorithm for stress update

The algorithm for stress update for an edge-shaped yield function is splitted in two parts: i) return to a side; and ii) return to an edge. For sides, the following system of equations has to be solved

$$\Delta \epsilon^p = \lambda_1 \frac{\partial g_1}{\partial \sigma} \quad (48)$$

$$\sigma = \hat{\sigma} - D : \Delta \epsilon^p \quad (49)$$

$$f_1(\sigma) = 0 \quad (50)$$

where λ_1 is the plastic multiplier, f_1 is the yield function and g_1 is the plastic potential of the side. If the final stress lands on an edge, eqns. (48) and (50) are replaced by

$$\Delta \epsilon^p = \lambda_1 \frac{\partial g_1}{\partial \sigma} + \lambda_2 \frac{\partial g_2}{\partial \sigma} \quad (51)$$

$$f_1(\sigma) = f_2(\sigma) = 0 \quad (52)$$

where g_2 is the plastic potential of the active edge, and λ_1, λ_2 are the non-negative multipliers.

The numerical implementation used in this paper is based (de Borst, 1987), (Souza Neto, Peric, & Owen, 2008). The proposed algorithm is performed in the invariant stress space with principal stresses ordered as $\sigma_1 < \sigma_2 < \sigma_3$.

The integration scheme is that of the implicit elastic predictor/plastic corrector algorithm as follows: It is assumed that σ lands on a side, the system defined by equations (48), (49), (50) is solved for σ . If $\sigma_1 < \sigma_2 < \sigma_3$, then σ is the updated stress. If not, it is assumed that σ lands on the triaxial compression edge, the system defined by equations (49), (51), (52) is solved for σ . If $\sigma_1 < \sigma_2 < \sigma_3$ then σ is the the updated stress. If not, it is assumed that σ lands on the triaxial extension edge, the same system is solved for σ . If $\sigma_1 < \sigma_2 < \sigma_3$ then σ is the the updated stress. Othewiese, the final stress state lies in the apex, therefore $\sigma = c_p \mathbf{1}$.

6.2 Flow rules

For the Vermeer-deBorst (VB) model, the plastic potential is defined as follows

$$g_1 = \sigma_3 - \sigma_1 + (\sigma_1 + \sigma_3) \sin(\psi) \tag{53}$$

$$g_2 = \sigma_2 - \sigma_1 + (\sigma_1 + \sigma_2) \sin(\psi) \tag{54}$$

$$g_3 = \sigma_3 - \sigma_2 + (\sigma_2 + \sigma_3) \sin(\psi) \tag{55}$$

Plastic strain rate tensors are

$$\mathbf{m}_1 = \{\sin(\psi) - 1, 0, \sin(\psi) + 1\} \tag{56}$$

$$\mathbf{m}_2 = \{\sin(\psi) - 1, \sin(\psi) + 1, 0\} \tag{57}$$

$$\mathbf{m}_3 = \{0, \sin(\psi) - 1, \sin(\psi) + 1\} \tag{58}$$

Decomposing each direction into its volumetric and deviatoric part yields

$$\mathbf{m}_i = \beta \mathbf{1} + \mathbf{m}_{di} \tag{59}$$

$$\beta = \frac{\sqrt{6} \sin(\psi)}{\sqrt{3 + \sin(\psi)^2}} \tag{60}$$

$$\mathbf{m}_{d1} = \{\sin(\psi) - 3, -2 \sin(\psi), \sin(\psi) + 3\} \frac{1}{\sqrt{6} \sqrt{\sin(\psi)^2 + 3}} \tag{61}$$

$$\mathbf{m}_{d2} = \{\sin(\psi) - 3, \sin(\psi) + 3, -2 \sin(\psi)\} \frac{1}{\sqrt{6} \sqrt{\sin(\psi)^2 + 3}} \tag{62}$$

$$\mathbf{m}_{d3} = \{-2 \sin(\psi), \sin(\psi) - 3, \sin(\psi) + 3\} \frac{1}{\sqrt{6} \sqrt{\sin(\psi)^2 + 3}} \tag{63}$$

For deviatoric associativity (DA), eqns. (36), (37) and (60) define the stress update. The deviatoric strain rate tensor reads like eqns. (61), (62) and (63) except for the fact that ϕ replaces ψ . In the case of radial return (RR), the plastic potential is a Drucker-Prager cone with aperture given by eqn (60). The deviatoric strain rate unit tensor is obtained from the deviatoric trial stress $\hat{\mathbf{s}}$

$$\mathbf{m}_d = \frac{\hat{\mathbf{s}}}{\|\hat{\mathbf{s}}\|} \tag{64}$$

Radial return, while most appealing from the numerical viewpoint, has not been used frequently as it has no physical background and might therefore produce non-physical results (Pivonka & Willam, 2003). Figure 7 shows the deviatoric section of the Hoek-Brown criterion along with the results obtained for different strain directions and the three flow rules employed.

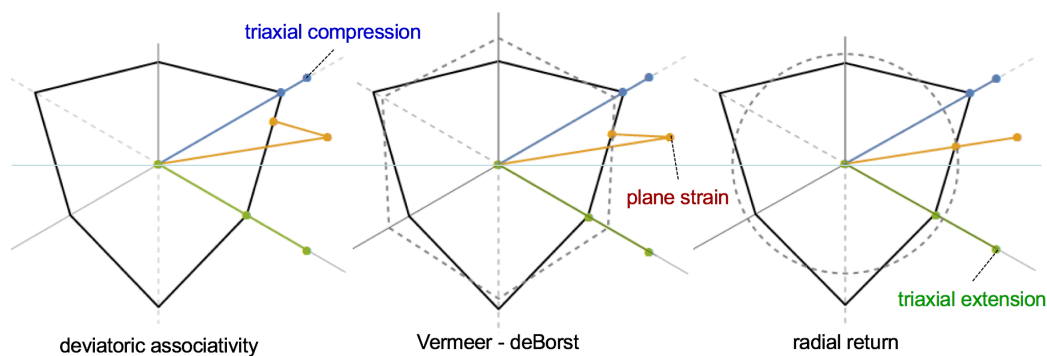


Figure 7: Deviatoric section on Hoek-Brown yield surface for three flow rules.

A numerical exercise is performed to investigate the implications of the choice of the flow rule on the results of the simulations. The focus is placed on the implications of the choice of the non-associativity model, keeping stress-dependent dilatancy switched-off and employing a constant dilatancy angle ψ . Figure 8 shows the deviatoric section of the Hoek-Brown criterion along with the stress updates obtained for different strain increments and $\psi = 0$.

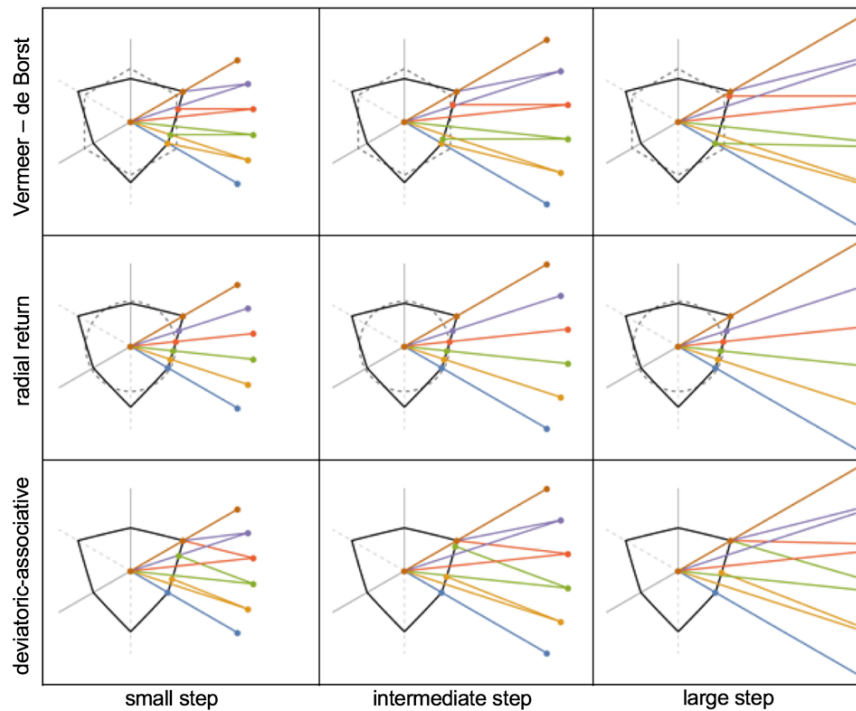


Figure 8: Deviatoric view of Hoek-Brown criterion and stress update for different strain increments, $\psi = 0$.

Several conclusions can be drawn from Figure 8: i) deviatoric associativity highly departs from Figure 5 close to the corners; ii) corners are attractors for both Vermeer-deBorst and deviatoric associative models; iii) radial return shows no corner attractor.

Choosing a flow rule by numerical convenience produces a strong and, sometimes, long standing impact. The industry seems to have arrived to the conclusion that J_3 yield criteria like Willam-Warnke, Lade-Duncan or Matsuoka-Nakai criteria add little value to Mohr-Coulomb or Hoek-Brown models, as all of them yield similar results. Whether this is a consequence of the choice of the flow rule should be further investigated. If eqn. (34) is used, stress updates move towards the triaxial compression or extension meridians of any curved yield surface, thus losing the augmented strength that would be otherwise predicted for plane-strain loading. Also, if the flow rule is just defined by using ψ instead of ϕ in any curved-shape J_3 yield function, $\psi \rightarrow 0$ implies radial return, as they all fall down to de Von Mises circle.

6.3 Stress update for the Hoek-Brown model

Having converted the Hoek-Brown criterion into a curved Mohr-Coulomb envelope, the standard integration of the Mohr-Coulomb model can be employed. The additional nonlinearity introduced by the dependence of ϕ on σ requires an iterative process, where Mohr-Coulomb parameters $c^{(i)}$ and $\phi^{(i)}$ are calculated for $\sigma_3^{(i)}$ and updated at each iteration (i) until convergence is obtained. The stress-update procedure described in Box 1 for the elementary case of constant dilatancy angle, where a constant slope in the $p - q$ plane.

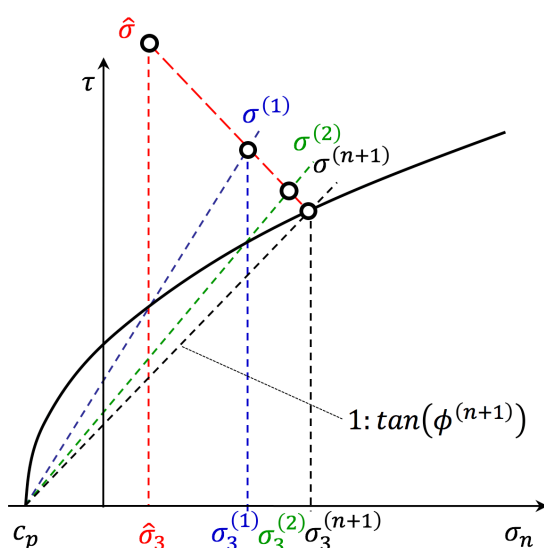


Figure 9: Stress update for Hoek-Brown model by iterating the Mohr-Coulomb model with $\phi(\sigma_3)$.

(i) From a converged state σ_n and strain increment $\Delta\epsilon$ evaluate the trial state

$$\hat{\sigma} = \sigma_n + D : \Delta\epsilon$$

(ii) Spectral decomposition. Compute eigenvectors $\{e_1, e_2, e_3\}$ and sort eigenvalues

$$\hat{\sigma}_1 < \hat{\sigma}_2 < \hat{\sigma}_3$$

(iii) Compute $\sin(\hat{\phi}) = 1/(1 + \omega(\hat{\sigma}_3))$

(iv) Compute the yield function

$$f_1 = \hat{\sigma}_3 - \hat{\sigma}_1 + \left(\hat{\sigma}_1 + \hat{\sigma}_3 - 2\sigma_c \frac{S}{m} \right) \sin(\hat{\phi})$$

IF $f_1 \leq 0$ THEN $\sigma = \hat{\sigma}$ and EXIT

(v) If $f_1 > 0$

a. Compute $\sigma_3^{(i=0)} = \hat{\sigma}_3$

b. Compute $\sin(\phi)^{(i)} = 1/(1 + \omega(\sigma_3^{(i)}))$

c. Update principal stresses using standard Mohr-Coulomb scheme

d. Update $\sin(\phi)^{(i+1)}$

e. Compute yield function

$$f = \sigma_3 - \sigma_1 + \left(\sigma_1 + \sigma_3 - 2\sigma_c \frac{S}{m} \right) \sin(\phi)^{(i+1)}$$

f. Loop until $\|f\| = 0$.

g. Switch-back to stress-space

$$\sigma = \sum_{i=1}^3 \sigma_i e_i \otimes e_i$$

Box 1: Stress update for the Hoek-Brown model.

7 VALIDATION

7.1 Plane-strain simulations

A plane-strain compression test was modeled to evaluate the response of all three mapping algorithms. All simulations were performed for a constant confining pressure of 10.0MPa, with the following material parameters: $\sigma_{ci} = 50 \text{ MPa}$, $m = 21.7$, $s = 0.45$, $a = 0.50$, $E = 4.8 \text{ GPa}$, $\nu = 0.20$. Results are summarized in Table 1.

The evolution of principal stresses with axial strain is shown in the left part of Figure 10, Figure 11 and Figure 12, whether the right parts show the evolution of stresses in the deviatoric plane together with the direction of the plastic strain increment.

For the VB model, the intermediate principal stress σ_2 depends solely on the elastic parameters of the model and thus stays stationary during plastic yielding. For both RR and DA models, σ_2 evolves during plastic shearing. In the case of DA, σ_2 eventually lands at the triaxial compression edge. The RR model shifts σ_2 towards the triaxial extension edge but reaches a stationary value which depends on all elastic and plastic parameters of the model.

| Flow rule | σ_1 [MPa] | σ_2 [MPa] | σ_3 [MPa] |
|-----------|------------------|------------------|------------------|
| VB | -119.4 | -31.9 | -10.0 |
| DA | -119.4 | -10.0 | -10.0 |
| RR | -119.4 | -66.7 | -10.0 |

Table 1: Principal stresses at failure for plane-strain simulations.

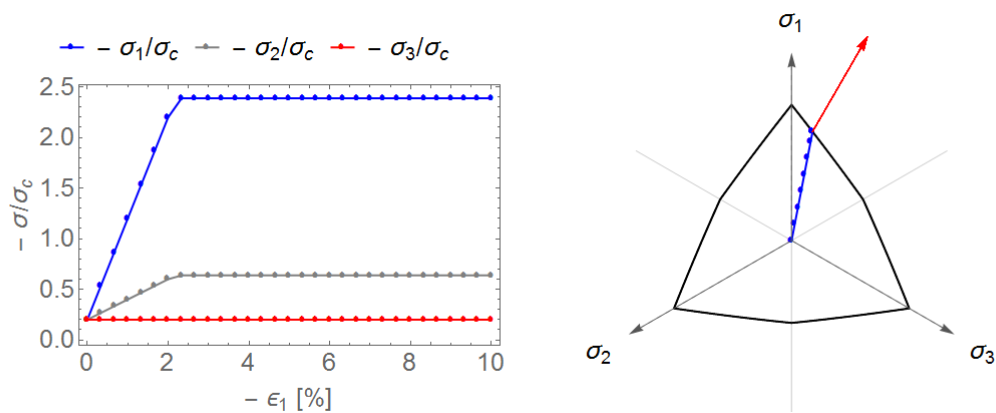


Figure 10: Plane-strain compression with Vermeer-deBorst flow rule.

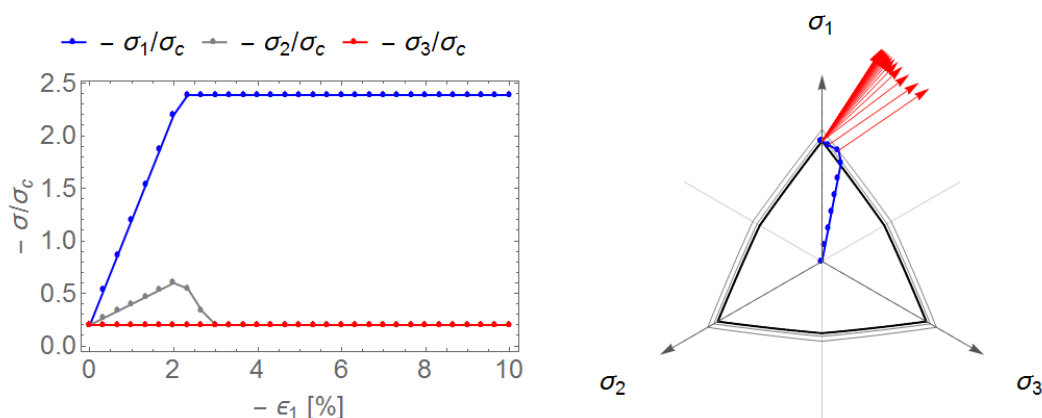


Figure 11: Plane-strain compression test with deviatoric associativity flow rule.

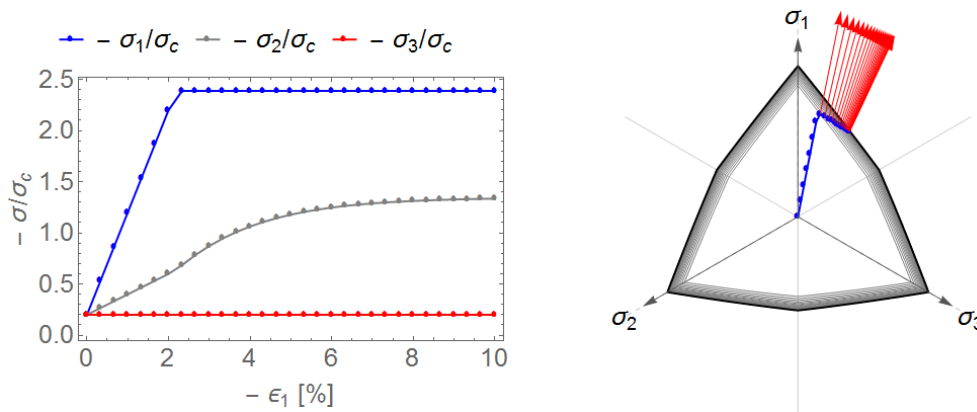


Figure 12: Plane-strain compression test with radial return flow rule.

A second exercise was performed to evaluate the impact of each flow rule on the factor of safety. The built-in Hoek-Brown model available in Plaxis 2D 2016 along with the VB, DA and RR models implemented as user-defined routines were employed. A maximum principal stress of 59.7MPa, approximately half of the yield stress, was applied. Then, the factor of safety was computed by the strength reduction technique.

The evolution of the factor of safety with the calculation steps is shown in Figure 13. Results are summarized in Table 2. A large amount of steps were required by the Plaxis built-in model to attain an stable F_n . On the contrary, the models presented here converged to a similar value for a small number of steps. It must be noted that the DA return shows a drop of F_n drops from 1.56 to 1.46 after sixty steps, when the condition $\sigma_2 = \sigma_3$ is reached.

| Flow rule | F_n |
|-----------------|-------------|
| Plaxis built-in | 1.48 1.52 |
| VB | 1.56 |
| DA | 1.46 |
| RR | 1.56 |

Table 2: Factor of safety calculation results, plane-strain compression test.

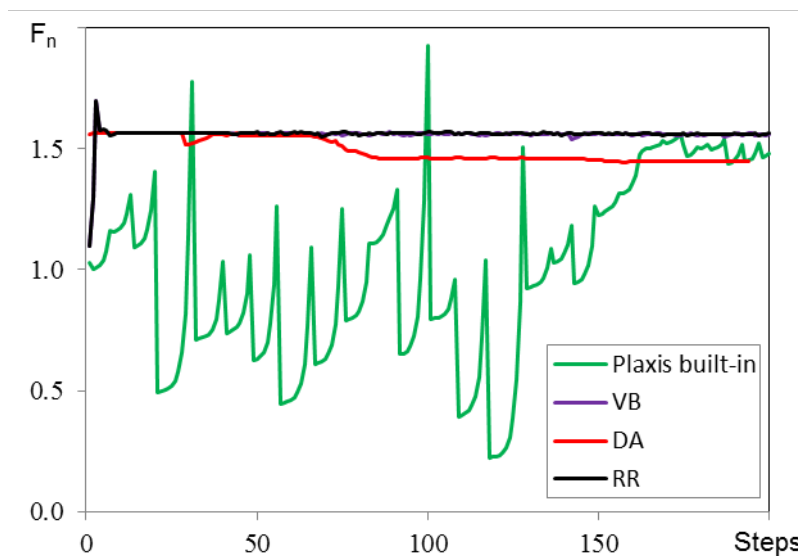


Figure 13: Factor of safety by the phi-c reduction technique, plane-strain compression test, Plaxis built-in Hoek-Brown model and this implementation for the three flow rules examined.

7.2 Slope stability

A numerical model of a slope excavated on a uniform material was performed using Plaxis. The mesh has 1155 15-node elements, 9367 nodes and an average element size of 9.5m. The slope is 100m high with an inclination of 63.43° . The finite element mesh is shown in Figure 14. Two Cases are examined with different strength parameters as summarized in Table 3. Elastic parameters are $E = 5.0 \text{ GPa}$, $\nu = 0.25$ and unit weight $\gamma = 25.0 \text{ kN/m}^3$. For each case, constant dilatancy angles of $\psi = 0^\circ$ and $\psi = 10^\circ$ were adopted.

| Case | σ_{ci} [MPa] | m | s | a |
|------|------------------------|-------|-----------------------|--------|
| 1 | 40 | 0.422 | 2.40×10^{-4} | 0.5057 |
| 2 | 40 | 1.231 | 2.90×10^{-3} | 0.5020 |

Table 3: Slope stability analysis. Material parameters for the two Cases studied.

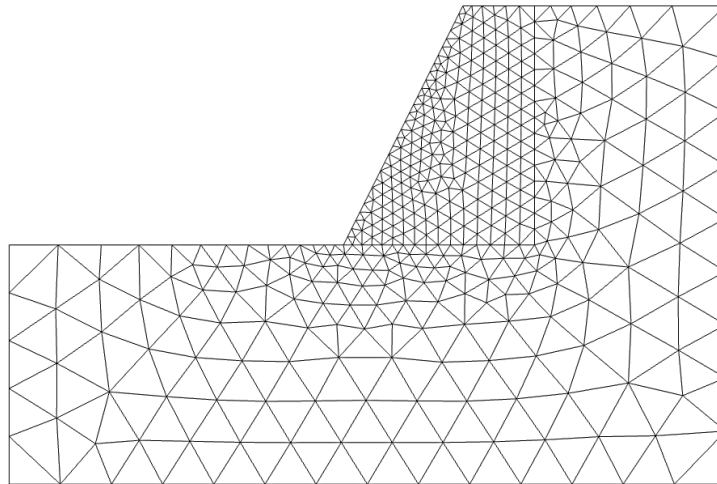


Figure 14: Finite element mesh for the slope stability exercise.

The factor of safety was calculated using the phi-c reduction routine available in Plaxis. Figure 15 depicts the evolution of F_n with calculation steps for the built-in phi-c reduction scheme from Plaxis, with $\psi = 0^\circ$. In Case 1, F_n drops to values close to zero. This is due to the fact that once a stress point lays in the apex, it remains locked there regardless of any changes in F_n . To avoid this issue, a small update on the constitutive models was performed, defining F_n as an additional model parameter. Then, simulations were run for different F_n values that were monotonically increased until convergence was no longer achieved. Results are summarized in Table 4 for different values of ψ .

Figure 16 shows the plastic points in the slope that results from both strategies. It is shown that, for the built-in phi-c reduction in Plaxis, a large portion of the plastic point are in tension failure (located at the apex), whether for the monotonic phi-c reduction scheme, a more defined failure surface develops with a few tension point at the top of the slope, as expected to be the realistic case.

For comparison purposes, a limit equilibrium analysis was performed using Slide V6.0 and Morgenstern-Price method, reaching $F_n = 1.31$ for Case ,1 and $F_n = 2.12$ for Case 2. It is shown that results from the finite element models are strongly influenced by the values of ψ . Results are close to the ones from limit equilibrium analyses, specially if the monotonic phi-c reduction implementation is used, with values of $\psi \approx 10^\circ$.

| Flow rule | Case 1 | | Case 2 | |
|-----------------|--|--|--|--|
| | Built-in phi-c reduction $\psi = 0^\circ \mid \psi = 10^\circ$ | User defined phi-c reduction $\psi = 0^\circ \mid \psi = 10^\circ$ | Built-in phi-c reduction $\psi = 0^\circ \mid \psi = 10^\circ$ | User defined phi-c reduction $\psi = 0^\circ \mid \psi = 10^\circ$ |
| Plaxis built-in | unstable | - | 1.85 1.85 | - |
| VB | unstable | 1.15 1.21 | 1.74 1.85 | 1.71 1.88 |
| DA | unstable | 1.11 1.21 | 1.74 1.91 | 1.71 1.92 |
| RR | unstable | 1.11 1.21 | 1.71 1.96 | 1.71 1.88 |

Table 4: F_n for both Cases using the built-in phi-c reduction scheme in Plaxis and a user defined version.

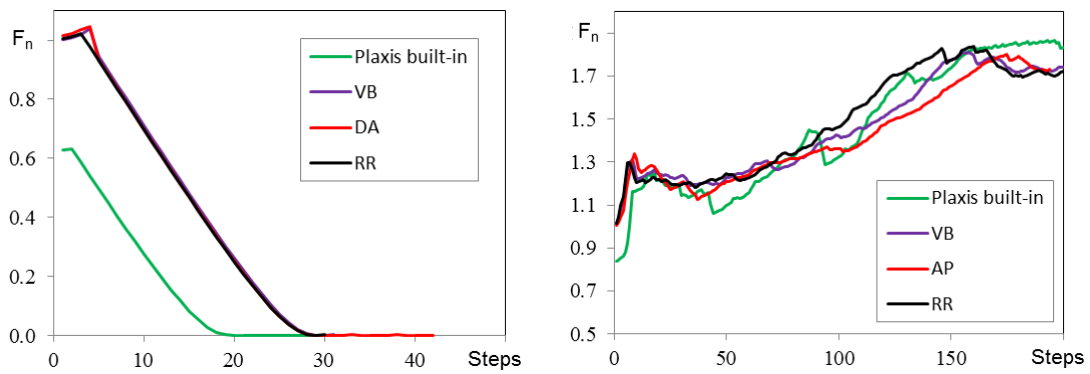


Figure 15: Factor of safety for the slope stability analysis. Case 1(left), Case2 (right). For both cases $\psi = 0^\circ$.

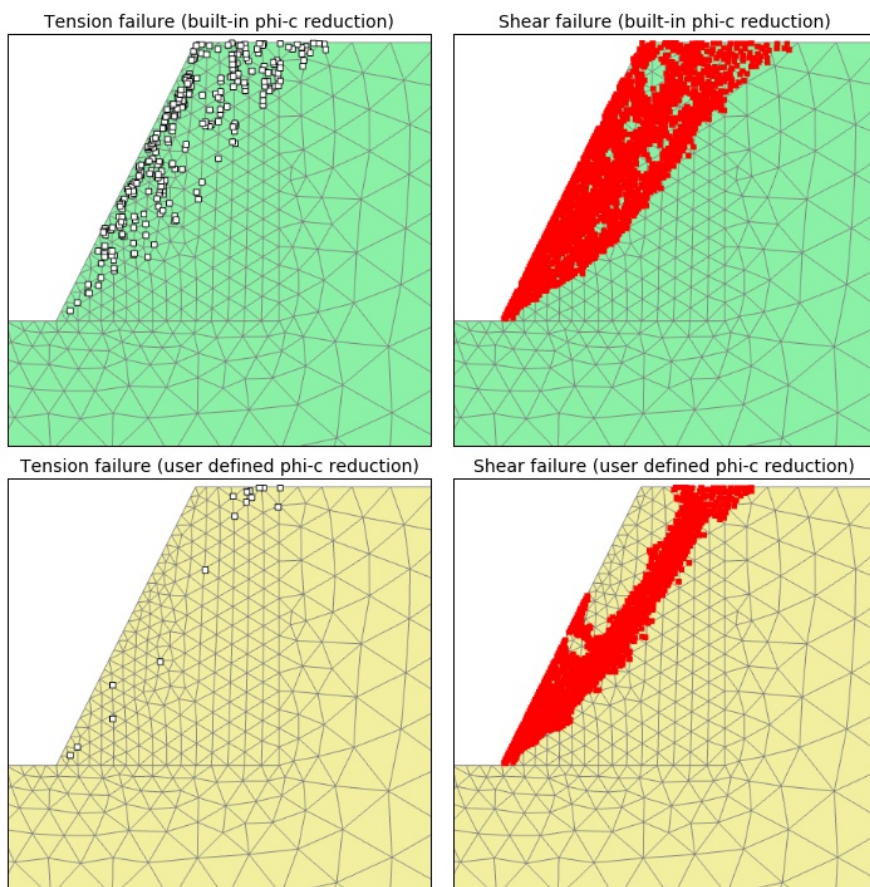


Figure 16: Plastic points at failure (white = tension; red = shear). Case 1 scenario with $\psi = 0^\circ$.

7.3 Open pit slope stability analysis

A numerical model of an open pit slope for a multipit mine in southern Argentina is presented. The slope is 130m high, with an overall slope of 59° and a 54° interramp. Benches are 20m high with 8m-wide berms. The mesh has 1375 15-node elements, with a total of 11159 nodes and an average element size of 17m. The finite element mesh is shown Figure 17.

The slope comprises three horizontal geotechnical domains, with thicknesses of 30m for material A and 73m for material B. Parameters are summarized in Table 5. Four constitutive models were considered: Hoek-Brown as defined in Plaxis, and the three flow rules for Hoek-Brown as defined herein. The excavation was modeled in seven stages 20m - high. The factor of safety was calculated for the final slope using the Plaxis built-in phi-c reduction scheme.

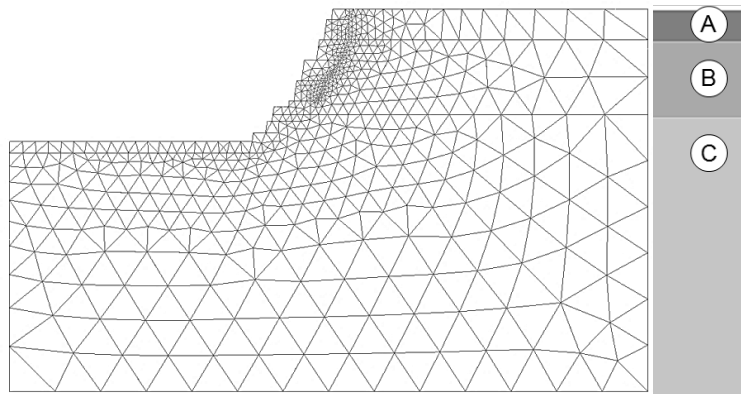


Figure 17: Finite element mesh and geotechnical domains for open pit slope.

Both DA and RR models yield higher F_n than the Plaxis built-in formulation, while simultaneously undergoing less ripple. Results are shown in Table 6. The kinematism shown in Figure 18, however, are similar. The VB model yields a much lower F_n with similar ripple, albeit with a quite different kinematism.

For completeness, a finite element model was performed using the different finite-element software RS². The mesh has 2959 6-node elements and 6014 nodes. Both $F_n = 3.16$ and the failure kinematism shown in Figure 19 compare closely with the DE and RR models and the Plaxis built-in formulation.

| Material | σ_c [MPa] | m [-] | s [-] | a [-] | E [GPa] | ν [-] | ψ [°] |
|----------|---------------------|------------|------------------------|------------|--------------|--------------|---------------|
| A | 21.6 | 3.007 | 6.738×10^{-3} | 0.5040 | 6.45 | 0.23 | 0 |
| B | 73.2 | 4.611 | 6.738×10^{-3} | 0.5040 | 9.19 | 0.23 | 0 |
| C | 73.2 | 3.857 | 3.866×10^{-3} | 0.5057 | 6.91 | 0.25 | 0 |

Table 5: Material parameters. Open pit slope.

| Flow rule | F_n |
|-----------------|-------|
| Plaxis built-in | 3.00 |
| VB | 2.74 |
| DA | 3.51 |
| RR | 3.50 |
| RS ² | 3.16 |

Table 6: F_n computed by phi-c reduction for different implementations of Hoek-Brown model and comparison with RS².

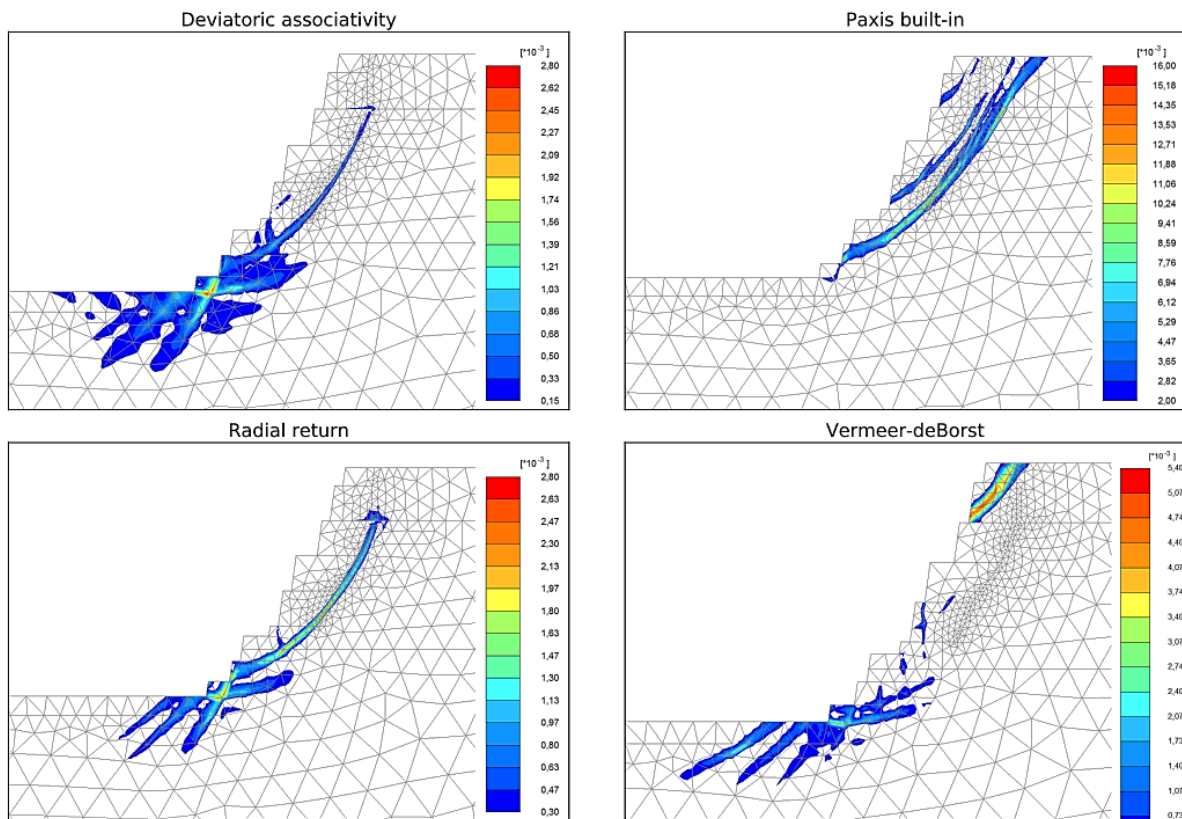


Figure 18: Deviatoric strains (left: DA Plaxis; right: RR). Computed values $F_n = 2.74|3.51$.

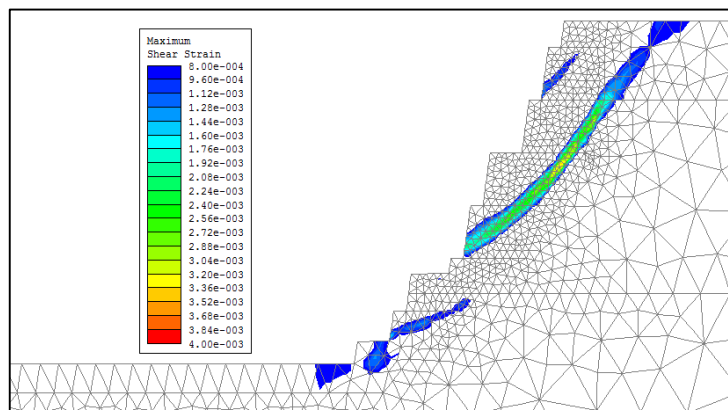


Figure 19: Deviatoric strains (RS²). Computed value $F_n = 3.16$.

7.4 Stress analysis of an underground excavation

A numerical model of an underground excavation for a transversal stopping mine in northern Uruguay is presented. The stope is 28m wide by 12m high, and is located 350m below ground surface. The model is 272m in width and 252m in height. The mesh has 1855 15-node elements, with a total of 14959 nodes and an average element size of 6.8m. The finite element mesh is shown in Figure 20.

The excavation was modeled in one stage. Boundary stresses were defined as $\sigma_y = 4.2\text{MPa}$ and σ_x varying between 7.1MPa at the uppermost and 17.3MPa and the lowermost end of the model. Again, the same four implementations of the Hoek-Brown model were employed. Material parameters are summarized in Table 7.

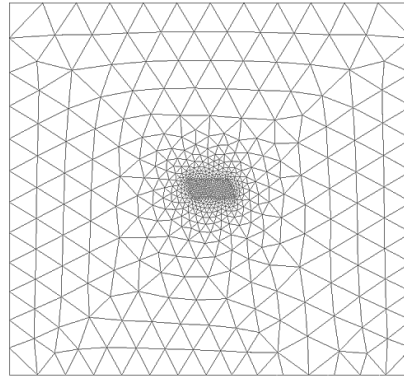


Figure 20: Finite element mesh for underground excavation.

| σ_c [MPa] | m [-] | s [-] | a [-] | E [GPa] | ν [-] |
|---------------------|------------|------------|------------|--------------|--------------|
| 150 | 9.791 | 0.1084 | 0.5006 | 20 | 0.25 |

Table 7: Material parameters. Underground excavation exercise.

The factor of safety was firstly calculated using the same phi-c reduction scheme for the built-in Hoek-Brown model with $\psi = 0^\circ$. Upon inspection of the F_n -steps curve, an intermediate kinematism was found at the 100th step with $F_n \approx 2.00$, consistent with a possible roof failure. Upon continuing the calculation, the factor of safety increased to $F_n = 5.49$, physically meaningless since the kinematism involved the whole model. The evolution curve of F_n together with the plastic point for each failure kinematism are shown Figure 21.

To investigate the stability of the excavation, the monotonic phi-c reduction scheme presented in this paper was employed. All three flow rules were analyzed with dilatancy angles of $\psi = 0^\circ$ and $\psi = 10^\circ$. Results are summarized in Table 8 and Figure 22. As expected for this kind of problem of a confined excavation, the dilatancy angle has a strong influence on F_n .

| Flow rule | F_n | |
|-----------------|------------------|-------------------|
| | $\psi = 0^\circ$ | $\psi = 10^\circ$ |
| Plaxis built-in | - | |
| VB | 2.03 | 2.52 |
| DA | 2.04 | 2.61 |
| RR | 2.06 | 2.61 |

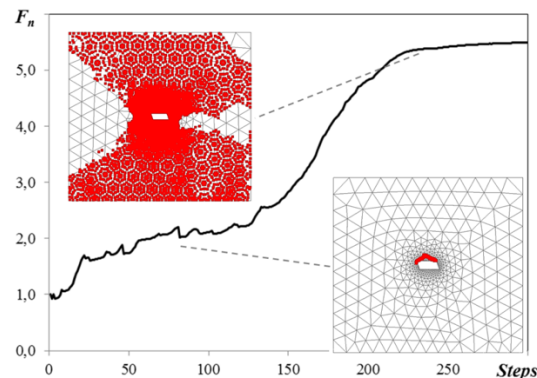
Table 8: F_n computed by the monotonic phi-c reduction technique.

Figure 21: Yielding points for two factors of safety (Plaxis built-in). Underground excavation.

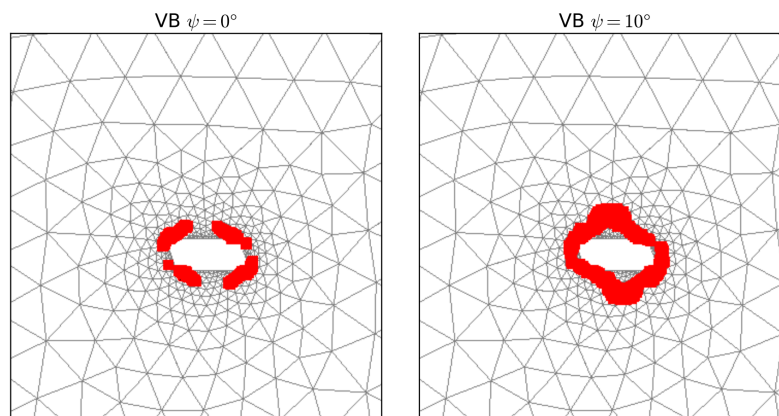


Figure 22: Plastic points for VB model and two values of ψ .

8 CONCLUSIONS

The Hoek–Brown model is found ubiquitously in engineering reports and employed for the computation of factors of safety by the strength reduction technique for a number of rock engineering designs. Unfortunately, the definition of the factor of safety for the Hoek-Brown criterion is not unique, thus yielding the comparison of values obtained by different codes useless.

In the first part of this paper, the Hoek-Brown model is rewritten as a Mohr-Coulomb model with a curved yield surface. This conversion allows for obtaining factors of safety that are entirely comparable to those of the Mohr-Coulomb criterion, on which most standards and codes are built. The paper also introduces the procedure to compute such factors of safety.

In the second part of the paper, the effect of the flow rule on the factor of safety is revisited. Three non-associativity formulations are discussed, implemented and compared to the built-in Hoek-Brown model available in Plaxis: deviatoric associativity & volumetric non-associativity, full non-associativity and radial return. It is shown that deviatoric associativity highly departs from experimental results and DEM simulations close to the edges of the Hoek-Brown yield surface, and that corners are attractors for both Vermeer-deBorst and deviatoric associative models but not for radial return. Simulations of plane-strain compression tests show that the implementation of the Hoek-Brown model presented in this paper shows a more stable behavior than the built-in model available in Plaxis for the computation of factors of safety. The exercise is repeated for the slope stability analysis of an uniform slope, showing that the dilatancy angle has an impact on the predicted factors of safety for all flow rules considered. Moreover, it is found that the built-in ϕ - c reduction scheme in Plaxis uses a non-monotonic reduction of strength parameters which severely undermine the numerical behavior of the models and might yield non-physical failure modes in some cases. The ϕ - c reduction scheme, rewritten to produce a monotonic reduction of strength parameters, is shown to overcome this issue.

In the third part of the paper, two case histories were analyzed. First, an open-pit rock slope was studied by employing all models described in the paper. It is shown that the flow rule does have an impact on the predicted failure kinematism, and that the dilatancy angle has a minor but noticeable effect. Finally, an underground excavation is modeled and the same analyses are performed for this second case. It is shown that the actual value of the dilatancy angle does have a heavy impact on the computed factor of safety, as expected for the constrained-type kinematism of an underground opening.

It is finally concluded that the Hoek-Brown implementation shown in this paper yields a robust and reproducible procedure for computing factors of safety in rock engineering, yielding results that are entirely comparable to prescribed values by codes and standards.

REFERENCES

- Benz, T., Schwab, R., Kauther, R. A., & Vermeer, P. A. (2008). A Hoek-Brown criterion with intrinsic material strength factorization. *International Journal of Rock Mechanics and Mining Sciences*, 45(2), págs. 210-222.
- Brinkgreve, R. B., Kumarswamy, S., & Swolfs, W. M. (2016). *Material Models Manual*. (P. BV, Ed.) Plaxis 2D version 2016.
- Collins, I. F. (2005). Elastic/plastic models for soils and sands. *International Journal of Mechanical Sciences*, 47(4-5), pp.493-508.
- de Borst, R. (1987). Integration of plasticity equations for singular yield functions. *Computers and Structures*, 26(5), págs. 823-829.
- Eberhardt, E. (2012). The Hoek-Brown failure criterion. *Rock Mechanics and Rock Engineering*, 45(6), págs. 981-988.
- Etse, G., & Willam, K. (1996). Integration algorithms for concrete plasticity. *Engineering Computations*, 13(8), pp.38-65.
- García Mendive, I., Sterin, U., & Rellan, G. S. (2016). Arenal Deep: application of numerical methods to two- and three- dimensional stability analyses of underground excavations. *Eurock 2016 (Capadocia, Turkey)*, p. 929-934.
- Guo, P., & Stolle, D. (2004). The extension of Rowe's stress-dilatancy model to general stress condition. *Soil Found*, 44(4):1-10.
- Guo, P., & Wan, R. (2007). Rational approach to stress-dilatancy modelling using an explicit micromechanical formulation. In *Bifurcations, Instabilities, Degradation in Geomechanics*, Springer, doi 10.1007/978-3-540-49342-6_10.
- Hammah, R. E., Yacoub, T. E., Corkum, B. C., & Curran, J. H. (2005). The Shear Strength Reduction Method for the Generalized Hoek-Brown Criterion. *40th U.S. Symposium on Rock Mechanics*, i. Alaska.
- Hoek, E., & Brown, E. T. (1980a). *Underground Excavations in Rock*. London Instn. Min. Metall.
- Hoek, E., & Brown, E. T. (1980b). Empirical strength criterion for rock masses. *J. Geotech. Engng Div. ASCE* 106, pp. 1013-1035.
- Hoek, E., Carranza, C., & Corkum, B. (2002). Hoek-brown failure criterion – 2002 edition. *NARMS-TAC Conference, 1*, págs. 267-273. Toronto.
- Itasca Consulting Group. (1998). *FLAC, Fast Lagrangian Analysis of Continua, Users Guide*. Minneapolis, Minnesota, USA.
- Kim, M. K., & Lade, P. V. (1988). Single hardening constitutive model for frictional materials I. Plastic potential function. *Comput Geotech*, 5:307-324.
- Macari, E. J., Weihe, S., & Arduino, P. (1997). Implicit integration of elastoplastic constitutive models for frictional materials with highly non-linear hardening functions. *Mechanics of Cohesive-frictional Materials*, 2, pp.1-29.
- Phusing, D., Suzuk, K., & Zaman, M. (2016). Mechanical Behavior of Granular Materials under Continuously Varying b Values Using DEM. *International Journal of Geomechanics*, 16.
- Pivonka, P., & Willam, K. (2003). The effect of the third invariant in computational plasticity. *Engineering Computations*, 20(5/6), pp.741-753.
- Rowe, P. (1962). The stress dilatancy relation for static equilibrium of an assembly of particles in contact. *Proc Royal Soc*, 269:500-527.
- Rowe, P. (1971). Stress - strain relationships for particulate materials at equilibrium. *Proc Perf Earth Earth Supported Struct*, 3:327-359.
- Sfriso, A. O. (2008). El coeficiente de seguridad en la geomcánica computacional. *CAMSIG*.
- Sfriso, A. O., & Weber, G. (2010). Formulation and validation of a constitutive model for sands in monotonic shear. *Acta Geotechnica*, 10.1007/s11440-010-0127-y.
- Sfriso, A. O., Weber, G., & Nuñez, E. (2011). Formulación de una regla de flujo no asociativa basada en la teoría de tensión-dilatancia de Rowe. *Revista Internacional de Desastres Naturales, Accidentes e Infraestructura Civil*, 12 (1) 19-26.
- Souza Neto, E., Peric, D., & Owen, D. R. (2008). *Computational Methods for Plasticity*. Wiley.
- Tsegaye, A. B., & Benz, T. (2014). Plastic flow and state-dilatancy for geomaterials. *Acta Geotechnica*, 9(2), 329-342.
- Zuo, Q. H., & Schreyer, H. L. (2010). Effect of deviatoric nonassociativity on the failure prediction for elastic-plastic materials. *International Journal of Solids and Structures*, 47(11-12), pp.1563-1571.